The Astrophysical Journal, 866:61 (7pp), 2018 October 10 https://doi.org/10.3847/1538-4357/aadc0c

Confirmation Of Two Galactic Supernova Remnant Candidates Discovered by THOR

Rohit Dokara[1], Nirupam Roy[1], Henrik Beuther[2], L. D. Anderson[3,4,5], Michael Rugel[2], Jeroen Stil[6], Yuan Wang[2], Juan D. Soler[2], and Russel Shanahan[6]
[1] Department of Physics, Indian Institute of Science, Bengaluru 560012, India; dokararohit@iisc.ac.in
[2] Max Planck Institute for Astronomy, Königstuhl 17, D-69117, Heidelberg, Germany
[3] Department of Physics and Astronomy, West Virginia University, Morgantown, WV 26506, USA
[4] Adjunct Astronomer at the Green Bank Observatory, P.O. Box 2, Green Bank, WV 24944, USA
[5] Center for Gravitational Waves and Cosmology, West Virginia University, Chestnut Ridge Research Building, Morgantown, WV 26505, USA
[6] Department of Physics and Astronomy, University of Calgary, 2500 University Drive NW, Calgary AB, T2N 1N4, Canada
Received 2018 April 9; revised 2018 August 13; accepted 2018 August 19; published 2018 October 11

Abstract

Anderson et al. identified 76 candidate supernova remnants (SNRs) using data from the H I/OH/Recombination line survey of the Milky Way. The spectral index and polarization properties can help distinguish between SNRs and H II regions, which are often confused. We confirm two SNR candidates using spectral index data and morphology. However, we observe that the fractional linear polarization cannot distinguish between SNRs and H II regions, likely due to contamination by diffuse Galactic synchrotron emission. We also comment on the association of SNR candidates with pulsars through geometric and age considerations.

Key words: ISM: H II regions – ISM: supernova remnants – polarization

1. Introduction

The list of nearly 300 Galactic supernova remnants (SNRs) compiled by Green (2014) is thought to be incomplete because it was estimated that there must be upwards of 1000 SNRs in the Milky Way (Li et al. 1991; Tammann et al. 1994). Even including recent TeV γ-ray SNRs detected by the High Energy Stereoscopic System (H.E.S.S.) collaboration does not increase this number greatly (Gottschall et al. 2017). Though the lack of detections at radio and X-ray wavelengths supports the arguments of Yamazaki et al. (2006) that there could be several SNRs with no radio, optical, ultraviolet, or X-ray emissions, Brogan et al. (2006) have shown that the deficiency is primarily due to the lack of sensitivity to observe low surface brightness SNRs and due to low angular resolution that prevents the detection of small angular size SNRs.

Galactic SNRs are routinely identified in radio wavelengths. The emission (or the lack of it) at different wavelengths depends on intrinsic factors, such as the progenitor's history, and also on external conditions, such as the properties of the surrounding medium. H II regions, which are bright at radio wavelengths due to thermal emission, are frequently confused with SNRs. SNRs have a significantly smaller ratio of flux at mid-infrared (mid-IR) wavelengths to flux at radio wavelengths than H II regions (Cohen & Green 2001). This feature led to the proposal of 76 candidate SNRs by Anderson et al. (2017) who have used radio continuum data from The H I/OH/Recombination line survey of the Milky Way (THOR; Beuther et al. 2016) and the Karl G. Jansky Very Large Array (VLA) 1.4 GHz Galactic Plane Survey (VGPS; Stil et al. 2006); and mid-IR wavelength data from *Spitzer* Galactic Legacy Infrared Midplane Survey Extraordinaire (GLIMPSE), *Spitzer* 24 and 70 Micron Survey of the Inner Galactic Disk with Multiband Infrared Photometer for Spitzer (MIPSGAL), and *Wide-field Infrared Survey Explorer* (*WISE*) surveys.

We propose confirming the identification of the candidate SNRs by measuring the fractional linear polarization and the spectral index of the total continuum emission. We measured these parameters for known SNRs and known H II regions in the THOR survey region ($|b| < 1.^{\circ}25$, $17.^{\circ}5 < l < 67.^{\circ}4$; see Beuther et al. 2016) and compared them with the data from candidate SNRs. The list of known H II regions was taken from the *WISE* catalog of Galactic H II regions (Anderson et al. 2014) through an interactive website (Anderson 2014). We leave out candidate H II regions and use only known H II regions with sizes greater than 1′, so that the comparison with known and candidate SNRs is appropriate.

Pulsars near the SNR candidates with associations to high-energy sources could be indicative of a positive identification. However, to ensure a clear identification, distances to the SNR and the pulsar should be compatible with age and proper motion of the pulsar. The Australia Telescope National Facility (ATNF) pulsar catalog (Manchester et al. 2005) provides the list of pulsars and their association with other sources.

H II regions are expected to have no linearly polarized emission at radio wavelengths because their emission is thermal. They have flat radio spectra ($\alpha \approx 0$)[7] for optically thin regions and $\alpha \gtrsim 0.5$ for optically thick regions.

On the other hand, SNRs are strong synchrotron sources, which are highly linearly polarized. For synchrotron emission in a uniform magnetic field, fractional linear polarization is related to the spectral index by (Wilson et al. 2013):

$$\Pi \equiv \frac{\sqrt{Q^2 + U^2}}{I} = \frac{3 - 3\alpha}{5 - 3\alpha}. \quad (1)$$

Synchrotron emission usually has $-2 < \alpha < 0$, so we expect fractional linear polarizations of above 0.6. However, we rarely observe $\Pi > 0.25$. This is due to the Faraday depolarization effect (Fletcher & Shukurov 2007). A varying rotation measure within the resolution element causes different Faraday rotations of the polarization vector, leading to a reduced polarization fraction being observed. As the polarization data from THOR is not yet fully processed (Beuther et al. 2016), we use the polarization data from the 1.4 GHz Northern VLA Sky Survey (NVSS; Condon et al. 1998).

[7] Spectral index α is defined by $S_\nu \propto \nu^\alpha$ for a flux density, S_ν, and a frequency, ν.

We use the publicly available spectral index map presented by de Gasperin et al. (2018), which is based on data from the 150 MHz TIFR GMRT.[8] Sky Survey (TGSS; Intema et al. 2017) and the NVSS.

Radio recombination lines (RRLs) are indicative of thermal processes, but the lines are often broad and weak. Beuther et al. (2016) have detected RRLs in the THOR survey only in some H II regions. Hence, while a detection of RRLs in THOR might imply thermal emission, a nondetection does not imply nonthermal emission, and it cannot be used to confirm the SNR candidates.

2. Data

2.1. List of Known and Candidate SNRs

The catalog by Green (2017) contains the list of all SNRs confirmed until 2016 along with their angular sizes. Of the 57 cataloged known SNRs in the THOR survey region, some SNRs are not visible in the 1.4 GHz THOR continuum data and some were classified as being H II regions by Anderson et al. (2017). Such objects are excluded from calculations, leaving us with 49 known SNRs. The list of SNR candidates is taken in its entirety from Anderson et al. (2017). Anderson et al. (2017) have combined the THOR 1.4 GHz continuum data (resolution $\sim 20''$) with VGPS data, which is called "THOR+VGPS." The combined THOR+VGPS data have a spatial resolution of $25''$. The THOR survey was taken by the VLA in C configuration, whereas VGPS was taken with the VLA in D configuration, and VGPS has single-dish continuum data added from the Effelsberg telescope (Stil et al. 2006).

2.2. NVSS

The NVSS covered entire sky north of $-40°$ decl. at 1.4 GHz, and its principal data products, maps of Stokes I, Q and U, are provided through a postage stamp server[9] (Condon et al. 1998). The compact D and DnC configurations of the VLA were used for the survey. Images were restored with a beam of $45''$. The largest angular scale detectable is about $8'$. The rms noise for Stokes I is ≈ 0.45 mJy beam^{-1}, and for Stokes Q, U is ≈ 0.29 mJy beam^{-1}. The noise in all Stokes maps can be higher in the Galactic plane by a factor of up to 1.5, depending on the observed region. We measured the source integrated flux density by retaining only those pixels above a 2.5σ level. To calculate polarized flux density, we apply this 2.5σ mask to the Stokes Q and U maps, and only those pixels above a 3σ level within this mask are retained. The NVSS contains blank pixels in some regions due to inadequate sky coverage and poor sensitivity. Four known SNRs, three SNR candidates, and 22 H II regions contain a large portion of blank pixels, in either Stokes I or Stokes Q and U. These objects are omitted in our calculations.

2.3. TGSS–NVSS Spectral Index Map

We utilize the pixel-by-pixel spectral index map[10] created using the 150 MHz TGSS and the 1.4 GHz NVSS by de Gasperin et al. (2018). The TGSS covers all sky north of $-53°$ decl. at 150 MHz with a resolution of $25''$. Intema et al. (2017) made an alternative release of the data collected by the TGSS team. The survey provides Stokes I images. The median rms noise is 3.5 mJy beam^{-1}. However, in the Galactic plane, the rms noise can be as high as 10 mJy beam^{-1}. For the TGSS, flux densities are well recoverable up to the order of a few arcminutes.

Similar to the NVSS, the TGSS is solely interferometric data and lacks single-dish data. Wezgowiec et al. (2016) have shown that for large structures (size $> 16'$), significant flux from extended regions is not detected in the NVSS data because of the limited spatial frequency coverage of the observations. Despite this problem, the use of these data together to measure spectral index is justified because the NVSS and the TGSS have similar shortest baselines and because they are two of the most sensitive centimeter and meter wavelength surveys with large sky coverage. Furthermore, our criterion to identify SNRs is based on a steep negative spectral index. If the flux undetected in the TGSS is indeed considerable, it would make the measured spectral index larger. Hence, the problem of undetected flux in the TGSS—if it exists—would make our criterion to detect SNRs even stronger.

Though spectral indices can be derived from the THOR data between 1000 and 2000 MHz (Bihr et al. 2016), the TGSS–NVSS spectral indices span an even broader frequency range of a factor of ~ 10 between 150 and 1400 MHz. These should be better suited for spectral index maps of SNR candidates with angular sizes of several arcminutes. At these scales, the THOR data are affected by generally stronger spatial filtering than the NVSS due to the more extended array configuration (VLA C configuration).

2.4. List of Known Pulsars and Their Associations

The ATNF pulsar catalog contains all known spin-powered pulsars and magnetars but excludes accretion-powered systems. The data is publicly available on the ATNF website[11] (Manchester et al. 2005). The list also provides distances, frequencies, and known associations of pulsars to SNRs, pulsar wind nebulae (PWNe), X-ray, and gamma-ray sources where available.

3. Results and Discussion

For the three samples (H II regions, known SNRs, and candidate SNRs), we have measured linearly polarized flux density, total flux density, and fractional linear polarization at 1.4 GHz from the NVSS and the 150–1400 MHz spectral index. A significant number of H II regions overlap with known and candidate SNRs. For instance, there are multiple bright H II regions in the shell-type SNRs G23.3−0.3 and G32.8−0.1. These introduce an uncertainty in both polarization and spectral index calculations. Unrelated sources, such as active galactic nuclei (AGN), also might affect the measurement of polarization and the spectral index. AGNs comprise most of the unrelated background sources. They are compact and have $\alpha \approx -1$.

3.1. Spectral Index

About 22% of known SNRs, ∼60% of SNR candidates, and ∼78% of H II regions are not detected in the TGSS. The TGSS is a snapshot survey with a large rms noise of ≈ 25 mJy beam^{-1} in the Galactic plane after convolving to the beam size of the NVSS. A pixel just above the detection limit in the NVSS data ($3\sigma = 1.35$ mJy beam^{-1}) will not be detected in the TGSS unless it has a steep negative spectral index (∼−1.8). A large fraction of SNRs, both known and candidate, are not detected

[8] Tata Institute of Fundamental Research (TIFR); Giant Metrewave Radio Telescope (GMRT).
[9] https://www.cv.nrao.edu/nvss/postage.shtml
[10] http://tgssadr.strw.leidenuniv.nl/doku.php?id=spidx#spectral_index_map
[11] http://www.atnf.csiro.au/research/pulsar/psrcat/

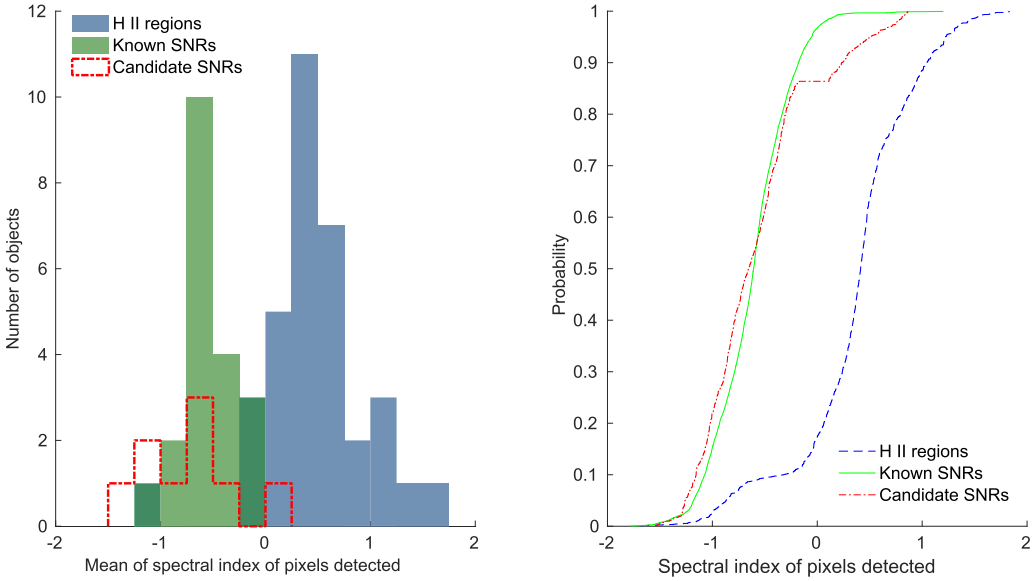

Figure 1. Left: distribution of the averages of spectral index values of pixels detected in both the NVSS and TGSS for the three samples. Right: cumulative probability distribution function of the spectral index of the pixels belonging to the three samples. Objects containing background sources and H II regions that overlap with known or candidate SNRs have been removed from the sample.

in the TGSS because they are not very bright at 1.4 GHz and do not have steep negative spectral indices.

The distribution of the spectral index of the three samples is shown in Figure 1. H II regions containing unrelated background sources or that overlap with possible or known SNRs have been removed from the sample. We find one anomalous H II region (G050.317−00.421) that has a large negative spectral index, consistent with the THOR continuum data (Bihr et al. 2016). This may be because of an AGN behind the H II region or because of contamination from diffuse synchrotron emission. SNRs that contain background sources were also removed from the sample. As expected, there is a separation in the spectral index distribution between thermal and nonthermal sources.

Only one candidate (G29.38+0.10) has a positive spectrum. It is indicative of a PWN, but no known pulsar exists along the direction of the central emission (Manchester et al. 2005).

The nonthermal spectral index from the shell can confirm the status of the candidates. Of the 76 candidates, only 3 have a clear partial shell structure with their spectral indices determined unambiguously: G27.06+0.04, G51.21+0.11, and G53.41+0.03. Several candidates, such as G17.80−0.02 and G36.68−0.14, have spectral indices from unidentified background sources. They have been excluded from the discussion.

3.1.1. Candidate G27.06+0.04

Two regions of this candidate are detected in all three surveys—the THOR, the NVSS, and the TGSS (Figure 2). The region to the southwest overlaps with the bright H II region G026.984−00.062, but it shows a nonthermal spectrum as well. The other region (eastern) has a partial shell morphology in THOR+VGPS data, and its nonthermal spectral index confirms its status as an SNR. A minor systematic gradient is present on the spectral index map of its shell, even after accounting for errors in the spectral index.[12] Similar gradients are observed in some other SNRs. This could be inherent due to spatially varying properties, such as optical depth and magnetic field, leading to a varied spectral index.

3.1.2. Candidate G51.21+0.11

Candidate SNR G51.21+0.11 was observed by Driessen et al. (2018) using the LOw Frequency ARray (LOFAR). They note that it has a morphology similar to the one found by Anderson et al. (2017). We argue that this candidate is a complex of two SNRs. The western region, named G51.04+0.07, was established by Supán et al. (2018) as a compact SNR. It is marked with a red circle in Figure 3.

A shell-type object centered at Galactic coordinates $l = 51.^{\circ}26$, $b = 0.^{\circ}11$ with a radius of $11.'3$ is visible in the THOR data. It is marked with a yellow circle in Figure 3. Thermal emission is detected at $l = 51.^{\circ}38$, $b = 0.^{\circ}00$. This thermal emission has RRLs in the THOR data (Beuther et al. 2016) and strong 8.0 μm mid-IR emission from GLIMPSE (Benjamin et al. 2003). This is due to an overlap with the shell of a candidate H II region, G051.457−00.286 (Anderson et al. 2014), which is marked with a cyan circle in Figure 3.

A nonthermal spectrum is detected from the eastern part of the shell at $l = 51.^{\circ}40$, $b = 0.^{\circ}08$. The shell lacks mid-IR emission from all regions other than the thermal emission mentioned above. The nonthermal spectral index from a part of the shell confirms its nature. Hence the originally defined candidate G51.21+0.11 is now reclassified as a complex of two objects: the compact SNR G51.04+0.07 (Supán et al. 2018) and the shell-type SNR G51.26+0.11.

3.1.3. Candidate G53.41+0.03

Driessen et al. (2018) confirmed the status of candidate SNR G53.41+0.03 using observations from LOFAR and *XMM-Newton*. Our findings—matching the partial shell shape in the NVSS, the TGSS, and the THOR data, and a nonthermal spectral index for the shell—agree with their classification.

[12] Available on http://tgssadr.strw.leidenuniv.nl/spidx/hips_spidxerr/ by de Gasperin et al. (2018).

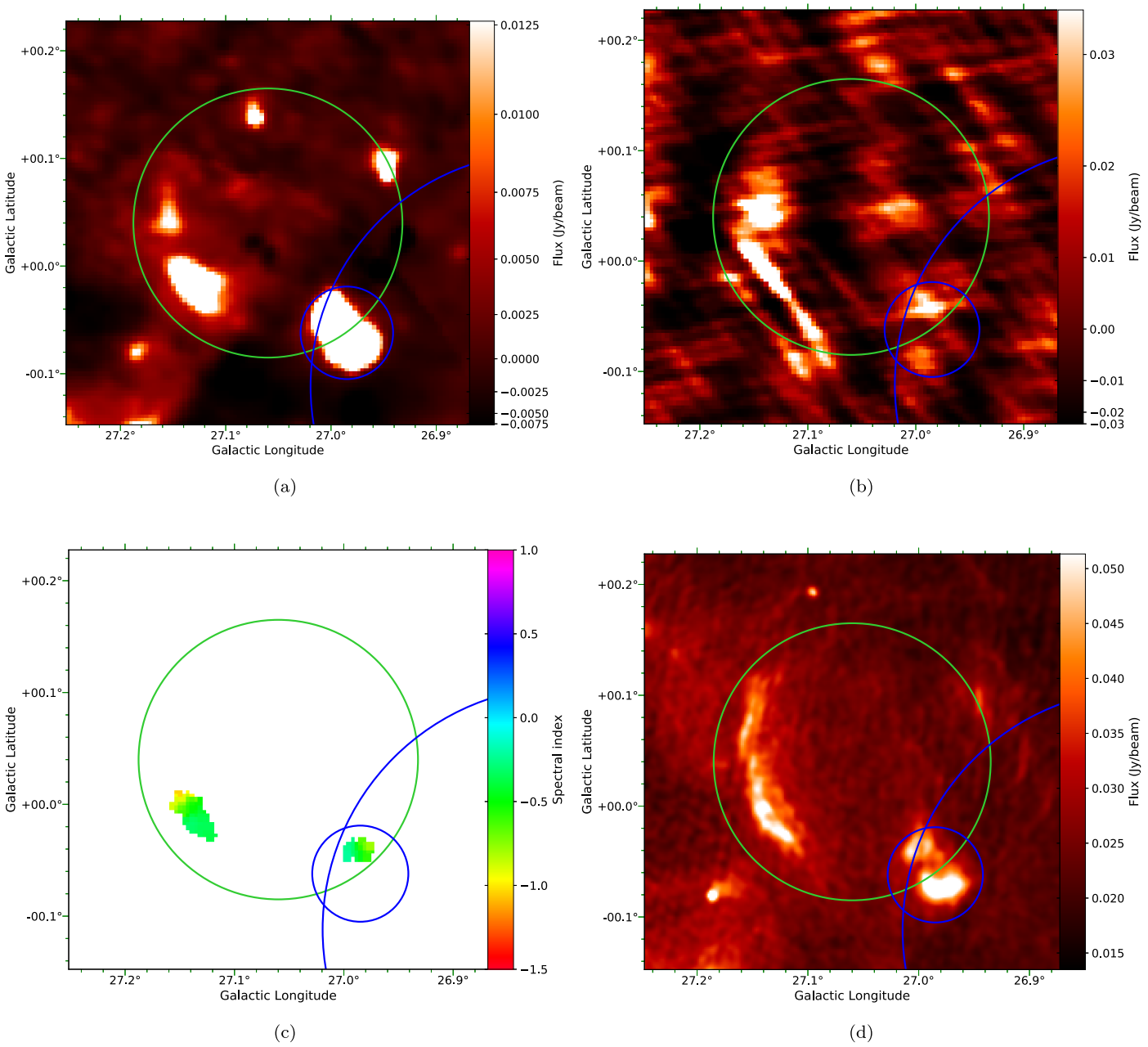

Figure 2. Candidate SNR G27.06+0.04: (a) NVSS 1.4 GHz Stokes *I*, (b) TGSS 150 MHz, (c) TGSS–NVSS spectral index map, and (d) THOR+VGPS 1.4 GHz. The candidate is enclosed by a green circle. H II regions are marked by blue circles.

3.1.4. Other Candidates with Nonthermal Spectra

The SNR candidate G28.78−0.44 has extended emission in both the NVSS and the TGSS data matching with the shell morphology in the THOR data and $\alpha \sim -0.75$. However, the spectral index was determined only for a small part of the shell. It is possible that an AGN is the cause of this spectral index. Hence we cannot confirm its status.

Compact SNR candidates G18.76−0.07, G58.70−0.75 and G59.68+1.25 have steep negative spectral indices, but we reserve judgment on those because of the lack of a shell morphology. We cannot rule out AGNs as the cause of these spectral indices.

The possible shell of PWN G54.1+0.3 (candidate SNR G54.11+0.25) is not visible in the TGSS data, consistent with the LOFAR observations of Driessen et al. (2018). We find only the PWN with $\alpha \sim -0.25$. Hence, we cannot comment on the status of candidate SNR G54.11+0.25. Anderson et al. (2017) and Driessen et al. (2018) discuss the possible shell around PWN G54.1+0.3.

3.1.5. Candidates with Lower Limits on Spectral Index

We note that if an object is detected in the NVSS but not in the TGSS, it does not necessarily mean that the object is not an SNR, since the lower limit on the spectral index for such pixels is ~ -1.2. Consider a typical pixel that is detected in the NVSS with a flux density of 5 mJy beam^{-1}, but not in the TGSS, which implies that its flux density at 150 MHz cannot be greater than $3\sigma_{\rm TGSS}$.[13] This gives a lower limit: $\alpha > -1.2$. The shells of

[13] $\sigma_{\rm TGSS} \approx 25$ mJy beam^{-1} in the Galactic plane after convolving TGSS images to the beam size of the NVSS.

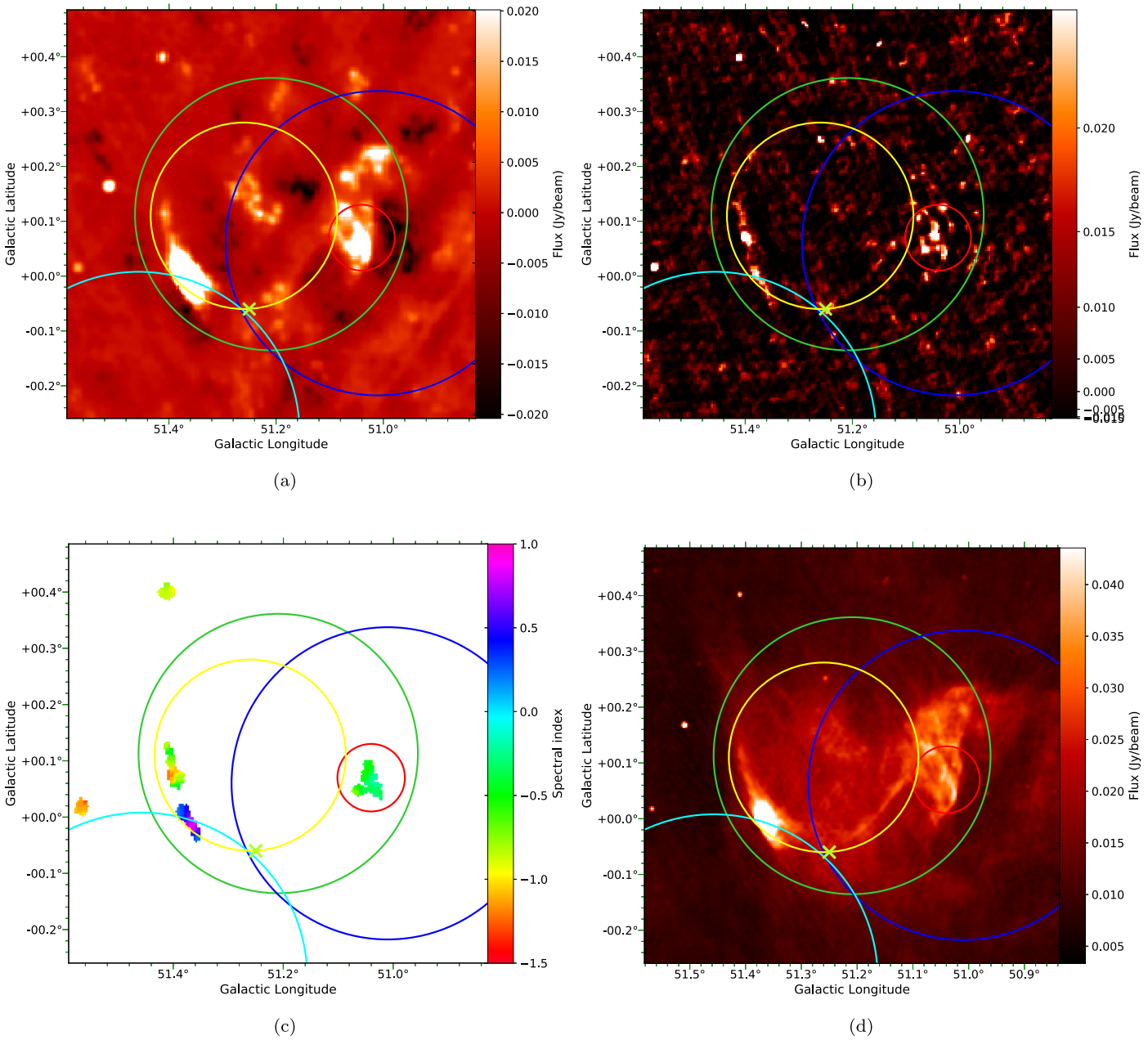

Figure 3. (a) NVSS 1.4 GHz Stokes *I*, (b) TGSS 150 MHz, (c) TGSS–NVSS spectral index map, and (d) THOR+VGPS 1.4 GHz. The extent of the following regions are marked by circles: candidate SNR G51.21+0.11 (green), H II region G051.010+00.060 (blue), candidate H II region G051.457−00.286 (cyan), SNR G51.26 +0.09 (yellow), and SNR G51.04+0.07 (red). PSR J1926+1613 is marked with a cross.

candidate SNRs G32.22−0.21 ($\alpha > -0.84$) and G36.68−0.14 ($\alpha > -0.67$)[14] are two examples. These limits, in general, are not helpful in identifying SNRs. We find one SNR candidate (G28.56 +0.00) with an interesting lower limit: $\alpha > 0.47$. This could be a misidentification by Anderson et al. (2017).

3.2. Polarization

Fractional linear polarization is plotted against NVSS flux density and its spectral index for the three samples (Figure 4). Polarization is higher for nonthermal sources as expected. We observe that there is no pronounced offset that distinguishes SNRs from H II regions, despite SNRs having higher polarization in general. This is due to polarization contamination. We do not attempt to correct for a polarization bias in this work. Estimating the noise in integrated Stokes *Q* and *U* maps of an extended source in the crowded Galactic plane is difficult. The small-scale structure in the polarization angle of unrelated diffuse Galactic emission acts as a non-Gaussian noise term that imposes its own bias on polarized intensity, resulting in apparent polarized signal from H II regions. Some or all of the higher degree polarization of fainter objects may be the result of a polarization bias.

3.3. Association with Pulsars

Possible associations of pulsars with SNR candidates could be used to argue for confirming the identification of SNR

[14] Obtained from the spectral index catalog—http://tgssadr.strw.leidenuniv.nl/doku.php?id=spidx#catalog.

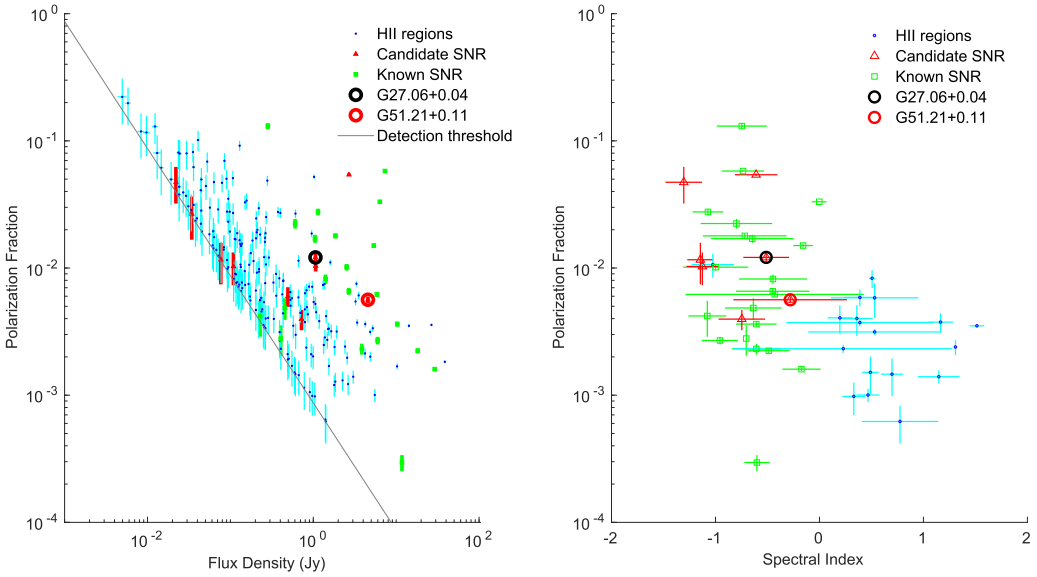

Figure 4. Left: fractional linear polarization against flux density from the 1.4 GHz NVSS data. The detection threshold is the lower limit of the polarization fraction that we can measure for a given flux density. Unpolarized sources are not shown. Right: fractional linear polarization against the mean of spectral index values detected.

candidates. The following conditions must be satisfied if a pulsar is associated with an SNR:

1. the distance estimates to the SNR and the pulsar should be compatible;
2. the age estimates of the SNR and the pulsar should be similar;
3. the pulsar should be young enough to harbor a radio remnant (i.e., age $\lesssim$100,000 years); and
4. the transverse motion of the pulsar should be such that it could have formed in the progenitor supernova explosion, and this transverse motion should give a reasonable estimate of the pulsar kick velocity.[15]

We identify 15 pulsars along the line of sight of 13 candidates. We do not have distance and age measurements of candidate SNRs, hence we cannot check for conditions (1) and (2). Only three pulsars (J1826−1256, J1838−0537, and J1930+1852) satisfy condition (3), of which one pulsar (J1838−0537) has no distance measurement in the ATNF pulsar catalog (Manchester et al. 2005).

Pulsar J1826−1256 is along the line of sight of candidate SNR G18.45−0.42. It is associated with a gamma-ray source (Nolan et al. 2012) and an X-ray source (Roberts et al. 2001). However, compared to the angular size of the candidate, the associated high-energy sources are too small to make a meaningful claim for an association. Given a distance of 1.55 kpc and an age of 14,400 years for pulsar J1826−1256 (Manchester et al. 2005), we find that the transverse kick velocity should be $\sim$210 km s^{-1} if candidate SNR G18.45−0.42 and the pulsar are indeed the results of the same supernova.

Pulsar J1930+1852 along the line of sight of candidate SNR G54.11+0.25 cannot be used to confirm the nature of the candidate due to its ambiguous shell (see Section 3.1.4; Anderson et al. 2017; Driessen et al. 2018).

[15] Pulsar kicks arise from asymmetry of the supernova explosion. The kick velocities typically range from 200 to 500 km s^{-1} (see Lai 2000, and references therein) but could be as high as $\sim$1100 km s^{-1} (Chatterjee et al. 2005).

4. Conclusions and Future Work

We have shown that the statistics of SNR candidates follows the sample of known SNRs more closely than that of H II regions in the spectral index and linear polarization. However, the fractional polarization could not be used to discriminate between SNRs and H II regions because of contamination by diffuse polarized emission in the Galactic plane. Compact sources and overlaps with known or candidate SNRs account for most of the steep negative spectra in H II regions. There is only one H II region, G050.317−00.421, with an apparent nonthermal spectrum that needs to be explained.

Despite the above shortcomings, spectral index data, along with morphology, confirmed the status of G27.06+0.04 and G51.26+0.11 as SNRs. There are three other candidate SNRs with nonthermal spectral indices (G18.76−0.07, G58.70−0.75, and G59.68+1.25) but with no shell morphology. High-energy emissions and a high degree of polarization might confirm their nature. Ongoing work on the THOR survey includes a careful analysis of the polarization data (J. Stil et al. 2018, in preparation). Though the THOR data are not ideal for deriving the spectra of large structures, they work well for compact sources (Bihr et al. 2016; Wang et al. 2018). Candidate SNRs G28.56+0.00 and G47.15+0.73 are such sources (angular size of $<3'$). They are detected in the 1.4 GHz NVSS but not in the 150 MHz TGSS. Future spectral index information from THOR could be used to study these candidates. Using optical emission lines could help to distinguish SNRs since they have elevated values for [S II]:Hα compared with H II regions, and the lines are often broader (Long et al. 2018).

We have been able to confirm the identification of only 2 candidates out of 76 using the spectral index and morphology. Several candidates have not been detected in the TGSS, and some have not been detected in the NVSS as well. Both these data are from snapshot surveys, which are not well suited to study low surface brightness emissions. On the other hand, compact candidate SNRs—despite favorable spectral index measurements—could not be confirmed because of confusion with background sources (AGNs). The low rate in confirming

the identification of candidate SNRs underlines the importance of future Galactic plane surveys with better sensitivity and high angular resolution.

We could not find any pulsar associations with candidate SNRs. More data on proper motions of pulsars, age, and distance measurements of candidate SNRs can be used to argue for or against an association. Proper motions of pulsars can be measured by comparing their current positions with the positions in the ATNF pulsar catalog. Distances to pulsars can be estimated from dispersion measure and an electron density model (Yao et al. 2017), or through the kinematic method. Astrometric observations by Very Long Baseline Array also can be used to measure parallaxes and proper motions of pulsars (Chatterjee et al. 2009).

R.D. is a recipient of INSPIRE scholarship from the Department of Science and Technology, Government of India. N.R. acknowledges support from the Infosys Foundation through the Infosys Young Investigator grant. H.B. and Y.W. acknowledge support from the European Research Council under the Horizon 2020 Framework Program via the ERC Consolidator Grant CSF-648505. This research has made use of NASA's Astrophysics Data System and data from surveys by VLA (run by the National Radio Astronomy Observatory) and GMRT (run by the National Centre for Radio Astrophysics of the Tata Institute of Fundamental Research). The National Radio Astronomy Observatory is a facility of the National Science Foundation operated under cooperative agreement by Associated Universities, Inc.

Software: ALADIN interactive sky atlas (Bonnarel et al. 2000), APLpy (Robitaille & Bressert 2012), SAOImage DS9 (Joye & Mandel 2003).[16]

ORCID iDs

Rohit Dokara https://orcid.org/0000-0002-1971-6725
Nirupam Roy https://orcid.org/0000-0001-9829-7727
Henrik Beuther https://orcid.org/0000-0002-1700-090X
L. D. Anderson https://orcid.org/0000-0001-8800-1793
Jeroen Stil https://orcid.org/0000-0003-2623-2064
Yuan Wang https://orcid.org/0000-0003-2226-4384

[16] http://ds9.si.edu/site/Home.html

References

Anderson, L. D. 2014, AAS Meeting, 223, 312.01
Anderson, L. D., Bania, T. M., Balser, D. S., et al. 2014, ApJS, 212, A1
Anderson, L. D., Bania, T. M., Balser, D. S., et al. 2014, yCat, 221, 20001
Anderson, L. D., Wang, Y., Bihr, S., et al. 2017, A&A, 605, A58
Benjamin, R. A., Churchwell, E., Babler, B. L., et al. 2003, PASP, 115, 953
Beuther, H., Bihr, S., Rugel, M., et al. 2016, A&A, 595, A32
Bihr, S., Johnston, K. G., Beuther, H., et al. 2016, A&A, 588, A97
Bonnarel, F., Fernique, P., Bienaymé, O., et al. 2000, A&AS, 143, 33
Brogan, C. L., Gelfand, J. D., Gaensler, B. M., et al. 2006, ApJL, 639, L25
Chatterjee, S., Brisken, W. F., Vlemmings, W. H. T., et al. 2009, ApJ, 698, 250
Chatterjee, S., Vlemmings, W. H. T., Brisken, W. F., et al. 2005, ApJL, 630, L61
Cohen, M., & Green, A. J. 2001, MNRAS, 325, 531
Condon, J. J., Cotton, W. D., Greisen, E. W., et al. 1998, AJ, 115, 1693
de Gasperin, F., Intema, H. T., & Frail, D. A. 2018, MNRAS, 474, 5008
Driessen, L. N., Domček, V., Vink, J., et al. 2018, ApJ, 860, 133
Fletcher, A., & Shukurov, A. 2007, EAS Publ. Ser., 23, 109
Gottschall, D., Capasso, M., Deil, C., et al. 2017, in AIP Conf. Proc. 1792, 6th Int. Symp. on High Energy Gamma-Ray Astronomy, ed. F. A. Aharonian, W. Hofmann, & F. M. Rieger (Melville, NY: AIP), 040030
Green, D. A. 2014, BASI, 42, 47
Green, D. A. 2017, yCat, 7278
Intema, H. T., Jagannathan, P., Mooley, K. P., & Frail, D. A. 2017, A&A, 598, A78
Joye, W. A., & Mandel, E. 2003, in ASP Conf. Ser. 295, Astronomical Data Analysis Software and Systems XII, ed. H. E. Payne, R. I. Jedrzejewski, & R. N. Hook (San Francisco, CA: ASP), 489
Lai, D. 2000, ASSL, 254, 127
Li, Z., Wheeler, J. C., Bash, F. N., & Jefferys, W. H. 1991, ApJ, 378, 93
Long, K. S., Blair, W. P., Milisavljevic, D., et al. 2018, ApJ, 855, 140
Lu, F. J., Wang, Q. D., Aschenbach, B., et al. 2001, ApJL, 568, L49
Manchester, R. N., Hobbs, G. B., Teoh, A., & Hobbs, M. 2005, AJ, 129, 1993
Nolan, P. L., Abdo, A. A., Ackermann, M., et al. 2012, ApJS, 199, 31
Prinz, T., & Becker, W. 2015, arXiv:1511.07713
Roberts, M. S. E., Romani, R. W., & Kawai, N. 2001, ApJ, 133, 451
Robitaille, T., & Bressert, E. 2012, Astrophysics and Source Code Library, APLpy: Astronomical Plotting Library in Python, ascl:1208.017
Stil, J. M., Taylor, A. R., Dickey, J. M., et al. 2006, AJ, 132, 1158
Supán, L., Castelletti, G., Peters, W. M., & Kassim, N. E. 2018, A&A, 616, 98
Tammann, G. A., Loeffler, W., & Schroeder, A. 1994, ApJS, 92, 487
Wang, Y., Bihr, S., Rugel, M., et al. 2018, arXiv:1808.05990
Wezgowiec, M., Jamrozy, M., & Mack, K.-H. 2016, AcA, 66, 85
Wilson, T. L., Rohlfs, K., & Huttemeister, S. 2013, Tools of Radio Astronomy (6th ed.; Berlin: Springer)
Yamazaki, R., Kohri, K., Bamba, A., et al. 2006, MNRAS, 371, 1975
Yao, J. M., Manchester, R. N., & Wang, N. 2017, ApJ, 835, 29